Monthly Notices
of the
ROYAL ASTRONOMICAL SOCIETY

MNRAS **472,** 3789–3804 (2017)
Advance Access publication 2017 August 26

doi:10.1093/mnras/stx2185

Dissecting the long-term emission behaviour of the BL Lac object Mrk 421

M. I. Carnerero,[1⋆] C. M. Raiteri,[1] M. Villata,[1] J. A. Acosta-Pulido,[2,3] V. M. Larionov,[4,5] P. S. Smith,[6] F. D'Ammando,[7,8] I. Agudo,[9] M. J. Arévalo,[2,3] R. Bachev,[10] J. Barnes,[11] S. Boeva,[10] V. Bozhilov,[12] D. Carosati,[13,14] C. Casadio,[15] W. P. Chen,[16] G. Damljanovic,[17] E. Eswaraiah,[16] E. Forné,[18] G. Gantchev,[12] J. L. Gómez,[9] P. A. González-Morales,[2,3] A. B. Griñón-Marín,[2,3] T. S. Grishina,[4] M. Holden,[19] S. Ibryamov,[10,20] M. D. Joner,[19] B. Jordan,[21] S. G. Jorstad,[4,22] M. Joshi,[22] E. N. Kopatskaya,[4] E. Koptelova,[16] O. M. Kurtanidze,[23,24,25] S. O. Kurtanidze,[23] E. G. Larionova,[4] L. V. Larionova,[4] G. Latev,[10] C. Lázaro,[2,3] R. Ligustri,[26] H. C. Lin,[16] A. P. Marscher,[22] C. Martínez-Lombilla,[2,3] B. McBreen,[27] B. Mihov,[10] S. N. Molina,[9] J. W. Moody,[19] D. A. Morozova,[4] M. G. Nikolashvili,[23] K. Nilsson,[28] E. Ovcharov,[12] C. Pace,[29] N. Panwar,[16] A. Pastor Yabar,[2,3] R. L. Pearson,[19] F. Pinna,[2,3] C. Protasio,[2,3] N. Rizzi,[30] F. J. Redondo-Lorenzo,[2,3] G. Rodríguez-Coira,[2,3] J. A. Ros,[18] A. C. Sadun,[31] S. S. Savchenko,[4] E. Semkov,[10] L. Slavcheva-Mihova,[10] N. Smith,[32] A. Strigachev,[10] Yu. V. Troitskaya,[4] I. S. Troitsky,[4] A. A. Vasilyev[4] and O. Vince[17]

Affiliations are listed at the end of the paper

Accepted 2017 August 21. Received 2017 August 21; in original form 2017 January 23

ABSTRACT

We report on long-term multiwavelength monitoring of blazar Mrk 421 by the GLAST-AGILE Support Program of the Whole Earth Blazar Telescope (GASP-WEBT) collaboration and Steward Observatory, and by the *Swift* and *Fermi* satellites. We study the source behaviour in the period 2007–2015, characterized by several extreme flares. The ratio between the optical, X-ray and γ-ray fluxes is very variable. The γ-ray flux variations show a fair correlation with the optical ones starting from 2012. We analyse spectropolarimetric data and find wavelength-dependence of the polarization degree (P), which is compatible with the presence of the host galaxy, and no wavelength dependence of the electric vector polarization angle (EVPA). Optical polarimetry shows a lack of simple correlation between P and flux and wide rotations of the EVPA. We build broad-band spectral energy distributions with simultaneous near-infrared and optical data from the GASP-WEBT and ultraviolet and X-ray data from the *Swift* satellite. They show strong variability in both flux and X-ray spectral shape and suggest a shift of the synchrotron peak up to a factor of ∼50 in frequency. The interpretation of the flux and spectral variability is compatible with jet models including at least two emitting regions that can change their orientation with respect to the line of sight.

Key words: galaxies: active – BL Lacertae objects: general – BL Lacertae objects: individual: Mrk 421 – galaxies: jets.

1 INTRODUCTION

The active galactic nuclei (AGNs) known as 'blazars are the ideal sources to study extragalactic jets, since in these objects one of the two jets coming out from the central black hole points towards us and its emission is thus enhanced by Doppler beaming. The low-energy

⋆ E-mail: maribel@oato.inaf.it

radiation that we observe from the radio to the optical–X-ray frequencies is ascribed to synchrotron radiation from relativistic electrons, while the highest energy radiation is most likely produced by inverse-Compton scattering on the same relativistic electrons. The photon seeds for the latter process can come either from the jet itself [synchrotron self-Compton (SSC) models] or from the disc, broad line region or torus [external Compton (EC) models]. High-energy radiation can also be produced by hadronic processes (Böttcher et al. 2013). At low frequencies, we can measure the degree and angle of polarization of blazar emission. The study of their variability and possible wavelength dependence is important to infer the jet properties because the polarization is tied to the jet magnetic field structure (e.g. Smith 1996; Visvanathan & Wills 1998).

Mrk 421 at $z = 0.031$ (Ulrich et al. 1975) is one of the best monitored blazar over the entire electromagnetic spectrum. It is classified as a high-energy-peaked BL Lac (HBL), which means that the synchrotron peak (and usually also the inverse-Compton peak) in its spectral energy distribution (SED) is positioned at relatively high frequencies.

It was the first blazar that was detected at energies $E > 500$ GeV (Punch et al. 1992), and many observing campaigns have recently been organized to analyse the source behaviour at TeV frequencies, usually including multiwavelength data (e.g. Aharonian et al. 2005; Albert et al. 2007; Donnarumma et al. 2009; Abdo et al. 2011; Aleksić et al. 2012, 2015a,b; Ahnen et al. 2016b; Baloković et al. 2016). It was observed by the Energetic Gamma Ray Experiment Telescope onboard the *Compton Gamma-Ray Observatory* with an average flux at $E > 100$ MeV of $(13.9 \pm 1.8) \times 10^{-8}$ photons cm^{-2} s^{-1} and a photon index $\Gamma = 1.57 \pm 0.15$ (Hartman et al. 1999). The *Fermi* Large Area Telescope (LAT) Third Source Catalog (Acero et al. 2015) reports a γ-ray flux of $\sim 18 \times 10^{-8}$ photons cm^{-2} s^{-1} between 100 MeV and 100 GeV, and a photon index $\Gamma = 1.77 \pm 0.08$. The source is very bright and variable at X-rays. In particular, a strong X-ray flare was observed in 2013 (Pian et al. 2014; Paliya et al. 2015; Sinha et al. 2015; Kapanadze et al. 2016). Optical observations have been available since 1899 (Miller 1975) and show that large-amplitude, rapid variability is a distinctive feature also in the optical band. The radio morphology reveals a bright nucleus and a one-sided jet with stationary or subluminal components (Piner, Pant & Edwards 2010; Blasi et al. 2013). An extreme radio flare was observed in 2012, possibly connected with preceding γ-ray flares (Hovatta et al. 2015). Possible radio–γ correlation was also found in 2011 by Lico et al. (2014).

In this paper, we analyse the Mrk 421 long-term flux and polarization behaviour. Very preliminary results were reported in Carnerero et al. (2016). We present the optical and near-infrared (near-IR) data obtained by the GLAST-AGILE Support Program (GASP) of the Whole Earth Blazar Telescope (WEBT) collaboration.[1] We compare the optical and near-IR flux variations with the X-ray and ultraviolet (UV) light curves obtained by the *Swift* satellite and with the γ-ray light curve from the *Fermi* satellite, by means of a cross-correlation analysis on the full data set available from 2007 to 2015. Moreover, we analyse the photopolarimetric behaviour and the spectropolarimetric data acquired at the Steward Observatory in the framework of the monitoring programme in support to the *Fermi* mission.[2] Finally, broad-band SEDs are built from the near-IR to the X-ray energies to investigate the source spectral variability in the synchrotron part of the spectrum.

2 OPTICAL PHOTOMETRY

Optical observations in *R* band for the GASP-WEBT were performed with 34 telescopes in 26 observatories around the world: Abastumani (Georgia), AstroCamp (Spain), Belogradchik (Bulgaria), Calar Alto[3] (Spain), Castelgrande (Italy), Crimean (Russia), L'Ampolla (Spain), Lowell (Perkins, USA), Lulin (Taiwan), New Mexico Skies (USA), Pulkovo (Russia), ROVOR (USA), Roque de los Muchachos (KVA and Liverpool, Spain), Rozhen (Bulgaria), SAI Crimean (Russia), Sabadell (Spain), Sirio (Italy), Skinakas (Greece), St. Petersburg (Russia), Talmassons (Italy), Teide (BRT, IAC80 and STELLA-I, Spain), Tijarafe (Spain), Torino (Italy), Tuorla (Finland), Astronomical Station Vidojevica - ASV (Serbia) and West Mountain (USA). Further *R*-band data were provided by the Steward Observatory (USA). Calibration of the source magnitude was obtained with respect to the reference stars 1, 2 and 3 by Villata et al. (1998).

The light curve in *R* band was built by carefully assembling the data sets coming from the different telescopes. Moreover, binning was used to reduce the noise of data acquired close in time by the same telescope. Offsets among different GASP data sets caused by partial inclusion of the host galaxy were minimized by adopting the same prescriptions for the photometry, i.e. an aperture radius of 7.5 arcsec. The Steward photometry was obtained with an extraction aperture of 7.6×10 arcsec^2, so that we had to add 2 mJy to the source flux density to make the Steward data match the GASP data.

The final light curve is shown in Fig. 1, where different symbols and colours highlight data from the various telescopes. It includes 5591 data points in the period from 2007 November 8 (JD = 2454412.7) to 2015 July 23 (JD = 2457227.4). They represent observed magnitudes, with no correction for the Galactic extinction and host-galaxy contribution. Strong variability characterizes the entire period on a large variety of time-scales.

3 NEAR-INFRARED PHOTOMETRY

The near-IR light curves of Mrk 421 in the period 2011–2015 are shown in Fig. 2 in *J*, *H* and *K* bands. The GASP-WEBT observations were performed by the 1.5-m TCS telescope in the Teide observatory.

The source calibration was obtained with respect to stars in the source field of view (FOV), whose magnitudes were adopted from the Two Micron All-Sky Data Release[4] (2MASS; Skrutskie et al. 2006). Because of the small FOV (4×4 arcsec^2) and consequent small number of reliable reference stars, we found a systematic offset between the zero-points of the Mrk 421 images with respect to the zero-points derived from the other fields images. We corrected for this difference and further checked that the inferred colour indices of the source were consistent with those reported in the 2MASS-point source catalogue.

As in the case of the optical data, the near-IR light curves were carefully checked and cleaned by reducing the data scattering through the binning of data close in time. These light curves are

[1] http://www.oato.inaf.it/blazars/webt/
[2] http://james.as.arizona.edu/~psmith/Fermi/
[3] Calar Alto data was acquired as part of the MAPCAT project: http://www.iaa.es/~iagudo/_iagudo/MAPCAT.html.
[4] http://www.ipac.caltech.edu/2mass/

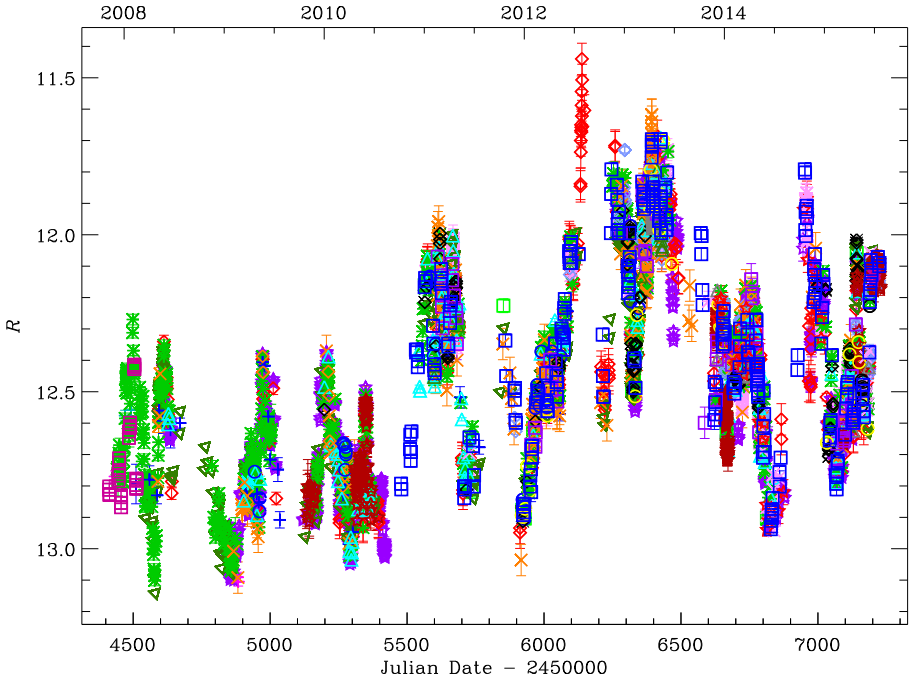

Figure 1. Optical light curve of Mrk 421 built with data from the GASP-WEBT collaboration and Steward Observatory in *R* band. Different colours and symbols highlight data from different telescopes. No correction for the host-galaxy contribution and Galactic extinction has been applied.

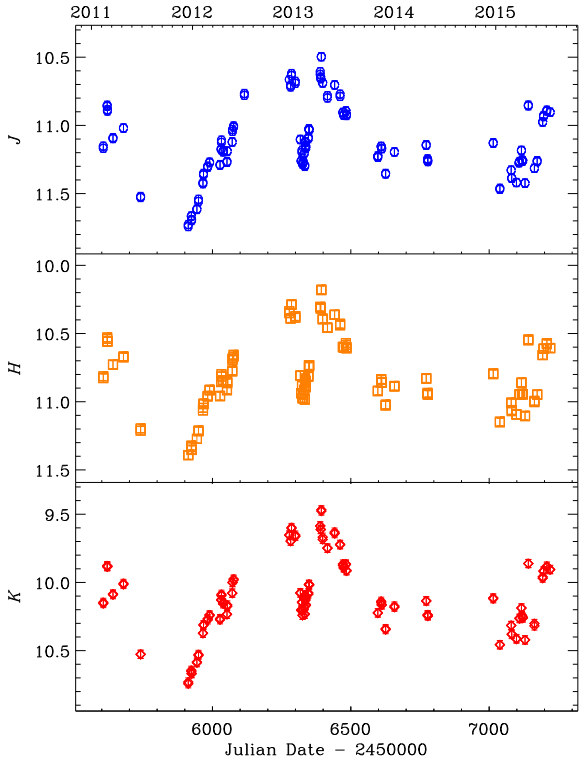

Figure 2. Near-IR light curves of Mrk 421 built with data from the GASP-WEBT collaboration in *J*, *H* and *K* bands. No correction for the host-galaxy contribution and Galactic extinction has been applied.

generally undersampled for a detailed comparison with the optical data, but where sufficient sampling has been achieved, they indicate that a close correspondence exists, as expected if the near-IR and optical emissions are produced by the same mechanism in the same jet region. We note that the amount of variability is nearly the same in the three near-IR bands.

4 REMOVAL OF THE HOST GALAXY CONTRIBUTION

The Mrk 421 host galaxy is relatively bright in optical bands, very strong in the near-IR, while its flux is small in UV bands. To remove the host-galaxy contribution, we used a de Vaucouleurs profile, as done by Raiteri et al. (2010) for BL Lacertae:

$$I(r) = I_{\rm e}\, {\rm e}^{-7.67[(r/r_{\rm e})^{0.25}-1]},$$

where $r_{\rm e}$ is the effective radius, i.e. the radius of the isophote containing half of the total luminosity, and $I_{\rm e}$ is the surface brightness at the effective radius. We used $r_{\rm e} = 8.2 \pm 0.2$ arcsec and $R_{\rm host} = 13.18$ mag (Nilsson et al. 2007) to estimate that the host galaxy contribution to the observed fluxes is $p = 48$ per cent of the whole galaxy flux with an aperture radius $r_{\rm a} = 7.5$ arcsec, as used by the WEBT observers. We also estimated $p = 37$ per cent for $r_{\rm a} = 5.0$ arcsec, the value that we will use in Section 6.1 for analysing the UV data (see Table 1).

In the *R* band, we found that 7.86 mJy must be subtracted from the observed photometric flux densities to isolate the non-thermal continuum of the active nucleus. We then calculated the host-galaxy contribution in the other bands by applying the colour indices determined by Mannucci et al. (2001) for elliptical galaxies to the de-reddened *R*-band magnitude. We adopted a Galactic extinction value of $A_R = 0.041$ mag from Schlegel, Finkbeiner & Davis (1998) and derived extinction in the other bands through the Cardelli, Clayton & Mathis (1989) laws, setting $R_V = A_V/E(B-V) = 3.1$, the mean value for the interstellar medium.

The optical and near-IR host magnitudes were converted into flux densities using the zero-mag fluxes given by Bessell, Castelli & Plez (1998). The whole galaxy flux densities were multiplied by

Table 1. UV, optical and near-IR observing bands with the corresponding Galactic extinction values A_λ, photometry aperture radius r_a, percentage of the host-galaxy flux included in the given aperture $p(r_a)$, host-galaxy flux density contribution to the source photometry F_{gal}, and median observed flux density $\langle F_\nu^{obs} \rangle$, including both Mrk 421 and the host galaxy.

Filters	A_λ (mag)	r_a (arcsec)	$p(r_a)$ (per cent)	F_{gal} (mJy)	$\langle F_\nu^{obs} \rangle$ (mJy)
$w2$	0.112	5.0	37	0.039	12.011
$m2$	0.118	5.0	37	0.067	14.305
$w1$	0.095	5.0	37	0.122	13.922
U	0.083	5.0	37	0.497	–
R	0.041	7.5	48	7.862	31.615
J	0.014	7.5	48	22.613	54.241
H	0.009	7.5	48	26.786	46.071
K	0.006	7.5	48	20.409	56.102

the $p(r_a)$ values to derive the contribution to the source photometry within the aperture radius. The results are shown in Table 1.

In the UV case, we used the template of a 13 Gyr elliptical galaxy that is available from the SWIRE project[5] (Polletta et al. 2007). We scaled the template in order to have the host-galaxy flux expected in the U filter. Galactic extinction in the UV bands was estimated by convolving the Cardelli et al. (1989) laws with the filter effective area and source spectrum. The results are in Table 1. As can be seen, the host galaxy contribution is relevant in the near-IR, whereas it is negligible in the UV.

We checked that using the SWIRE Template method to calculate the host galaxy contribution at lower frequencies gives the same results obtained by the colour indices method within a few mJy.

5 COLOUR ANALYSIS

Analysis of colour variations is an important tool to investigate the spectral behaviour of the source and, in turn, the nature of its emission.

In Fig. 3, we show the J-band light curve (top panel) together with the corresponding $J-K$ colour indices as a function of time (middle panel) and brightness level (bottom panel). The colour indices were calculated by selecting J- and K-data points with small errors and taken within at most 15 min. We obtained that the average $J-K$ value is 1.12, with a standard deviation of 0.05. The data were corrected for the host galaxy contribution as explained in Section 4.

It can be seen that, in general, the values of $J-K$ decrease with increasing flux, which is more evident in the bottom panel, where the behaviour of the colour index with brightness is displayed. We observe a bluer-when-brighter trend, as expected for a BL Lac object (e.g. Ikejiri et al. 2011), with a linear Pearson's correlation coefficient of 0.79 and Spearman's rank correlation coefficient of 0.77.

6 OBSERVATIONS BY *SWIFT*

In this section, we analyse the *Swift* satellite data on Mrk 421 obtained with the UV/Optical Telescope (UVOT; Roming et al. 2005) and X-ray Telescope (XRT; Burrows et al. 2005) instruments. During the 2007–2015 period, the source was observed by *Swift* in 727 epochs.

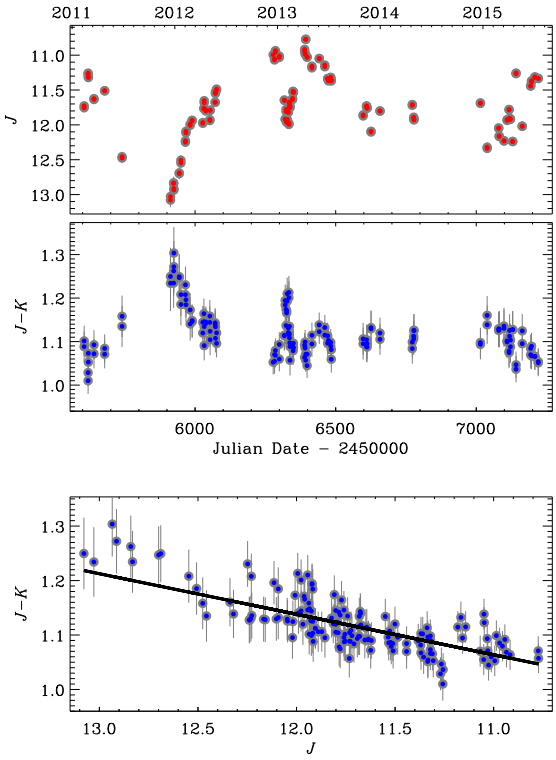

Figure 3. The J-band light curve in the 2011–2015 period (top panel); the corresponding $J-K$ colour index as a function of time (middle panel) and brightness level (bottom panel). In the bottom panel, the solid line represents a linear fit to the data. The data have been corrected for the host galaxy contribution.

6.1 UVOT

The UVOT instrument on board *Swift* observed Mrk 421 mostly in the UV bands $w1$, $m2$ and $w2$, and sometimes also in the optical bands v, b, u. We downloaded these data from the NASA's High Energy Astrophysics Science Archive Research Center (HEASARC)[6] and reduced them with the HEASOFT package version 6.17 and the calibration release 20150717 of the CALDB data base available at HEASARC. For each epoch, multiple images in the same filter were first summed with the task `uvotimsum` and then aperture photometry was performed with `uvotsource`. We extracted source counts from a circular region with 5 arcsec radius centred on the source and background counts from a circle with 15 arcsec radius in a source-free field region.

The UVOT light curves are shown in Fig. 4. They confirm the general behaviour shown by the ground-based optical and near-IR curves in Figs 1 and 2.

6.2 XRT

We processed the XRT data with the HEASOFT package version 6.17 and the CALDB calibration files updated 20150721. The task XRTPIPELINE was executed with standard screening criteria. Only observations performed in pointing mode and with more than 50 counts were selected for further analysis. In the 2007–2015 period, we were left with 710 observations in windowed timing (WT) mode

[5] http://www.iasf-milano.inaf.it/polletta/templates/swire_templates.html

[6] http://heasarc.nasa.gov

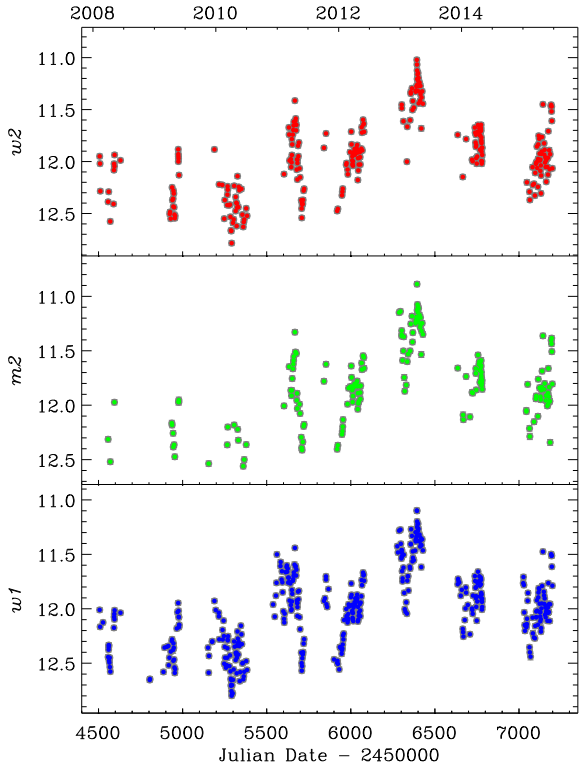

Figure 4. UV light curves of Mrk 421 built with *Swift*-UVOT data.

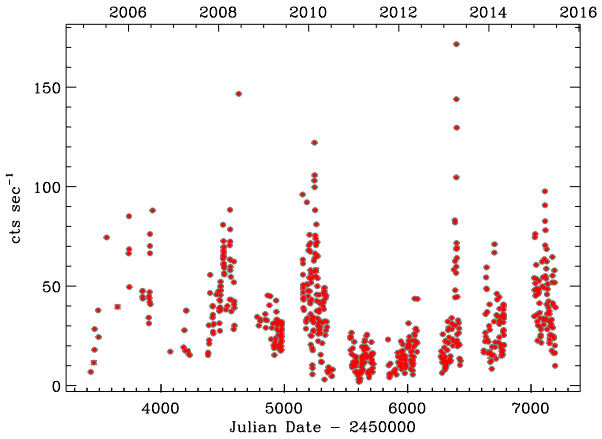

Figure 5. X-ray light curve of Mrk 421 obtained from data collected by the XRT instrument onboard the *Swift* satellite in the period 2007–2015.

and only 16 in photon counting mode, so that we concentrated on the former.

We selected event grades 0–2 and used a circular region with 70-arcsec radius centred on the source to extract the source counts, and a similar region shifted away from the source along the window to extract the background counts. We verified that the background is negligible, as background counts are in average 1.5 per cent and at maximum 5 per cent of the source counts, so we did not correct for it. Only three observations in WT mode have a mean rate greater than 100 counts s^{-1}, implying pile-up. To correct for pile-up, we discarded the inner 3-pixel radius circle in the source extraction region.

We used the XRTMKARF task to generate ancillary response files (ARF), which account for different extraction regions, vignetting

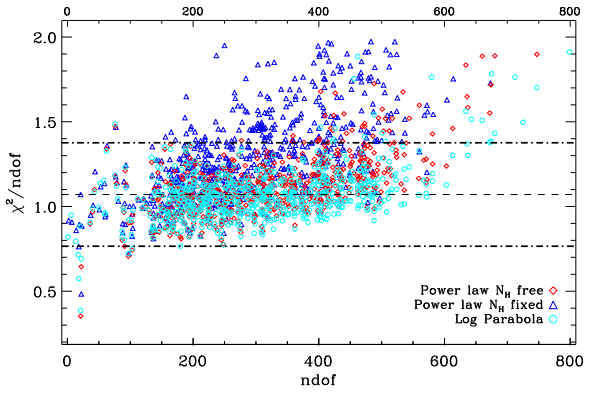

Figure 6. Reduced χ^2 versus the ndof for the different models applied to the XRT spectra of Mrk 421. Blue triangles represent the results of the power-law model with N_H fixed to the Galactic value, red diamonds those of the power-law model with N_H free and the cyan circles those of the log-parabola model with Galactic N_H.

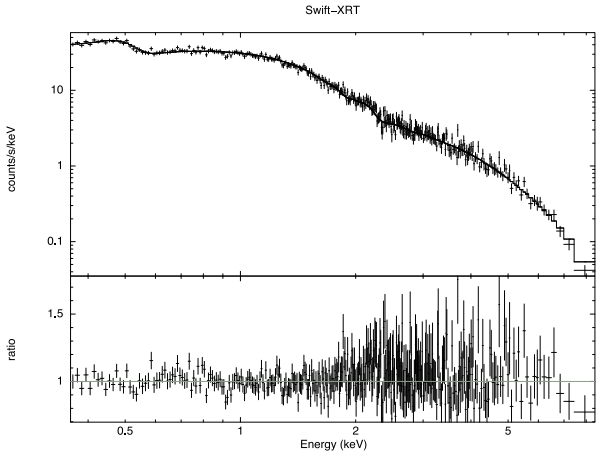

Figure 7. The XRT spectrum of Mrk 421 on 2008 February 13. The best fit was obtained with a log-parabola model. The bottom panel shows the ratio of the data to the folded model.

and PSF corrections. The X-ray light curve is shown in Fig. 5 and is discussed in the next Section.

By means of the task *grppha*, we associated the source spectra with the ARF and CALDB redistribution matrix function files, and binned the source spectra in order to have a minimum of 20 counts in each bin for the χ^2 statistics. These grouped spectra were then analysed with the XSPEC package, using the energy channels greater than 0.35 keV to improve the goodness of the fit.

We applied three different models for the spectral fitting: (1) an absorbed power-law model, where absorption is modelled according to Wilms, Allen & McCray (2000) and the hydrogen column is fixed to the Galactic value $N_H = 1.61 \times 10^{20}$cm^{-2}, as derived from the 21-cm measure by Lockman & Savage (1995); (2) an absorbed power-law model with N_H free; and (3) an absorbed log-parabola model with N_H fixed to the Galactic value. We favoured the third model, whose χ^2 is usually smaller than that of the other models, and that produces results with smaller errors. In Fig. 6, we show the χ^2 versus the number of degrees of freedom (ndof). The χ^2 is more stable when the log-parabola model is applied, but it increases with ndof. This is possibly due to a pronounced curvature. Fig. 7 shows an example of XRT spectrum. It was best fitted with a log parabola.

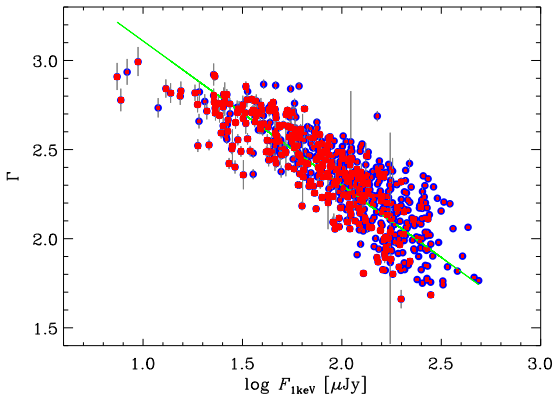

Figure 8. The X-ray photon index Γ as a function of the unabsorbed flux density at 1 keV. Data with error less than 30 per cent of the flux are shown. Red squares refer to the best-fitted cases, where the reduced χ^2 is in the range 0.8–1.2 and the ndof is >10. The solid line represents a linear fit to the data.

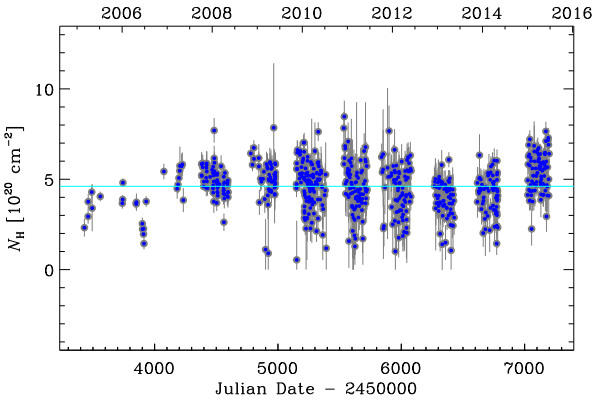

Figure 9. The Galactic hydrogen column N_{H} as a function of time when a power-law model with free absorption is applied to the XRT spectra. The cyan line marks the average value.

In the case of a power-law model with fixed N_{H}, the photon index Γ ranges from 1.66 to 2.99, indicating a spectrum that oscillates from hard to soft. The average value is 2.34, with standard deviation of 0.26. To understand whether these spectral changes correspond to real variations or are due to noise, we recall the definition of the mean fractional variation $F_{\mathrm{var}} = \sqrt{\sigma^2 - \delta^2}/\langle f \rangle$ (Peterson 2001), which is commonly used to characterize variability. Here, $\langle f \rangle$ is the mean value of the variable we are analysing, σ^2 its variance and δ^2 the mean square uncertainly. In our case, $F_{\mathrm{var}} = 0.11$, so we conclude that the variations reflect genuine source variability rather than noise. Fig. 8 displays the photon index Γ as a function of the flux density at 1 keV. We note that the lowest Γ values correspond to the highest fluxes, in agreement with the harder-when-brighter trend often observed in blazars. However, this model produces statistically unacceptable fits (see Fig. 6).

On the other hand, the power-law model with N_{H} free implies a large spread of N_{H} values, which very unlikely corresponds to a physical scenario (see Fig. 9). We note that in this case the mean value of N_{H} exceeds the Galactic value by a factor of ∼3, suggesting that the spectrum is curved.

The log-parabola model has largely been used to fit the X-ray spectrum of this source (e.g. Massaro et al. 2004; Sinha et al. 2015). It offers a statistically better fit to the data in case of a curved spectrum. In this model, the photon index Γ is replaced by two parameters: α, the photon index, and β, the spectral curvature. We obtained α values in the range from 1.58 to 2.99, similar to that found for Γ in the power-law case. The average value is 2.27, with standard deviation of 0.28. The mean fractional variation is $F_{\mathrm{var}} = 0.12$. The β parameter goes from −0.09 to 0.66, with an average value of 0.24 and standard deviation of 0.10. The mean fractional variation is $F_{\mathrm{var}} = 0.29$. The large range of β values indicates strong curvature changes. However, large uncertainties affect the most extreme β values, demanding caution.

In Fig. 10, we show the trend of the α and β parameters of the log-parabola model applied to the X-ray spectra of Mrk 421 as a function of the source flux. While α behaves similarly to Γ (Fig. 8), confirming the harder-when-brighter spectral property, no clear correlation between β and flux is recognizable. We obtained a linear Pearson's correlation coefficient of 0.86/0.20 and Spearman's rank correlation coefficient of 0.88/0.16 for the α/β cases.

7 OBSERVATIONS BY *FERMI*

The LAT (Atwood et al. 2009) instrument onboard the *Fermi* satellite observes in the 20 MeV–300 GeV energy range. In this paper, we considered data between 2008 August 4 (JD = 2454683.15) and 2015 September 10 (JD = 2457275.50). We used Pass 8 data (Atwood et al. 2013), based on a complete revision of the entire LAT event-level analysis. We adopted the SCIENCETOOLS software package version v10r0p5 and followed the standard reduction procedure, as done in Carnerero et al. (2015). We considered a region of interest of radius 30°, a maximum zenith angle of 90° and only 'Source' class events (evclass=128, evtype=3). The spectral

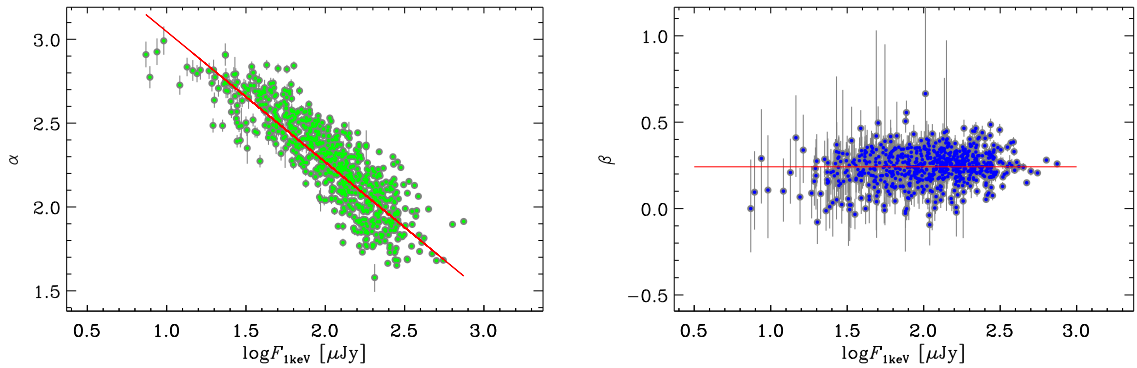

Figure 10. The behaviour of the α (left-hand panel) and β (right-hand panel) parameters of the log-parabola model applied to the XRT spectra of Mrk 421 as a function of the unabsorbed flux density at 1 keV. The solid lines represent linear fits to the data.

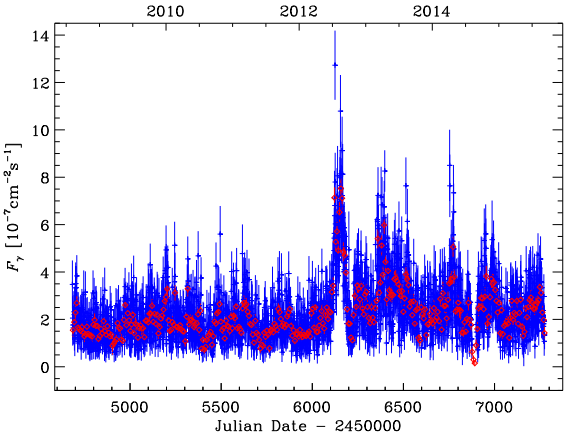

Figure 11. The *Fermi*-LAT 0.1–300 GeV fluxes (10^{-7} photons cm^{-2} s^{-1}) derived with different time bins in the 2008–2015 period (red symbols refer to weekly binned data and blue symbols to daily binned data).

analysis was performed with the science tool `gtlike` and the response function P8R2_SOURCE_V6. Background was modelled with isotropic (iso_source_v06.txt) and Galactic diffuse emission (gll_iem_v06.fit) components.

As in the 3FGL catalogue, we used a power-law model for the Mrk 421 spectrum. A first maximum likelihood analysis was performed over the whole period to remove from the model the sources having Test Statistics[7] less than 10. A second maximum likelihood was run on the updated source model.

Integrating over the whole period, the fit gives TS = 111714 in the 0.1–300 GeV energy range, with an integrated average flux of $(2.18 \pm 0.02) \times 10^{-7}$ photons cm^{-2} s^{-1} and a photon index $\Gamma = 1.77 \pm 0.01$. The high statistical significance allowed us to obtain weekly binned and even daily binned light curves, which are displayed in Fig. 11. The spectral indices of Mrk 421 and all sources within 10° were frozen to the values resulting from the likelihood analysis over the entire period.

8 MULTIWAVELENGTH BEHAVIOUR

Fig. 12 compares the time evolution of the Mrk 421 flux at different frequencies in the 2007–2015 period. The 2013 outburst was observed at all frequencies, while the X-ray outbursts in 2008 and 2010 lack a major optical counterpart (and the latter also a γ counterpart) and are difficult to identify in UV because of sparse sampling. In contrast, in 2011, we notice a flare in UV, optical and near-IR, but not in X-rays and γ-rays. In γ-rays, a major outburst is observed in 2012, at the same time of the strongest optical event. Other noticeable γ-ray flares were detected in 2013 and 2014. In general, the source behaviour at γ energies appears similar to that observed in the optical band, while the X-ray light curve seems quite different (see also Donnarumma et al. 2009).

In Fig. 13, we compare the source behaviour in X-ray and *R* band. The long-term trend is traced by means of cubic spline interpolations through the 15-d binned light curves. The ratio between the X-ray and optical splines is displayed in the bottom panel and highlights that the X-ray emission strongly dominates from 2007 June to 2009 June, its importance decreases from 2009 June to 2010 July, and

[7] This is defined as: TS = $2(\log L_1 - \log L_0)$, where L_1 and L_0 are the likelihood of the data when the model includes or excludes the source, respectively (Mattox et al. 1996).

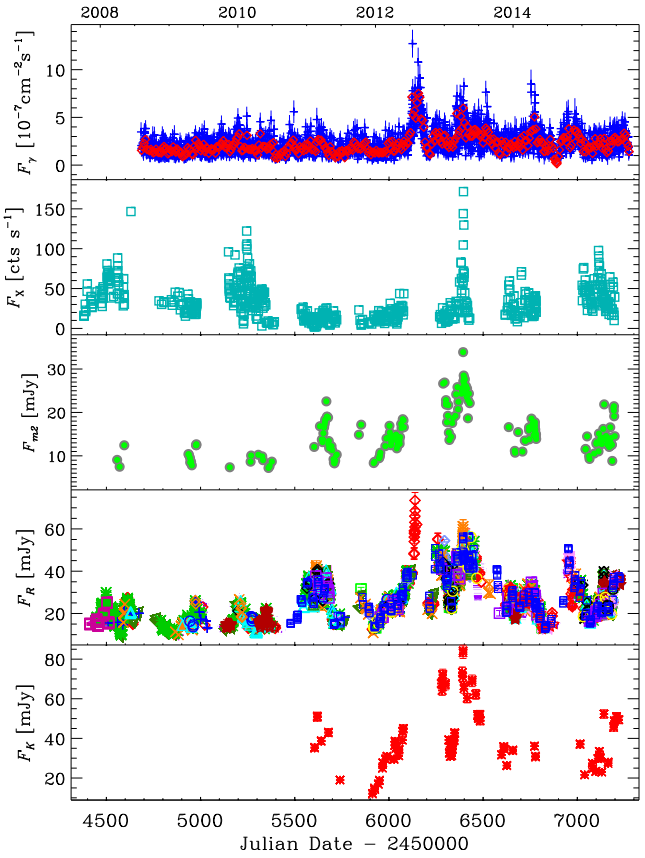

Figure 12. Multiwavelength emission behaviour of Mrk 421 as a function of time. From the top to bottom: the γ-ray fluxes in the 100 MeV–300 GeV energy range from *Fermi*, red diamonds/blue plus signs refer to weekly/daily binned data; the X-ray count rate from *Swift*-XRT; the *Swift*-UVOT observed flux densities in the *m*2 band (mJy); the *R*-band observed flux densities (mJy); and the *K*-band observed flux densities (mJy). Data in the *m*2, *R* and *K* filters were cleaned from the host-galaxy light contamination.

reaches a minimum in 2010 October–2012 June, when the source is very active in the optical band. Starting from 2013, the ratio appears to moderately increase again.

In HBLs, the optical and X-ray emissions are thought to be both produced by synchrotron process. The variability of the X-ray-to-optical flux ratio in Mrk 421 then may indicate that the jet zones from where the X-ray and optical radiations are emitted do not coincide and are characterized by their own short-term variability. Moreover, the fact that periods of X-ray flux dominance alternate with periods of optical flux dominance suggests that the corresponding emitting regions belong to a curved jet whose orientation changes may alternatively favour the Doppler enhancement of one region with respect to the other (e.g. Villata et al. 2009a,b). An alternative explanation would be that of a one-zone model where the jet parameters change so that the synchrotron peak frequency shifts, modifying the ratio between the X-ray and optical fluxes. However, this kind of model met some difficulties in explaining the behaviour of Mrk 421 during the 2008 active state (e.g. Aleksić et al. 2012).

9 VARIABILITY OF THE OPTICAL POLARIZATION

As mentioned in the Introduction, the polarized blazar emission shows a variable degree of linear polarization (*P*) and electric

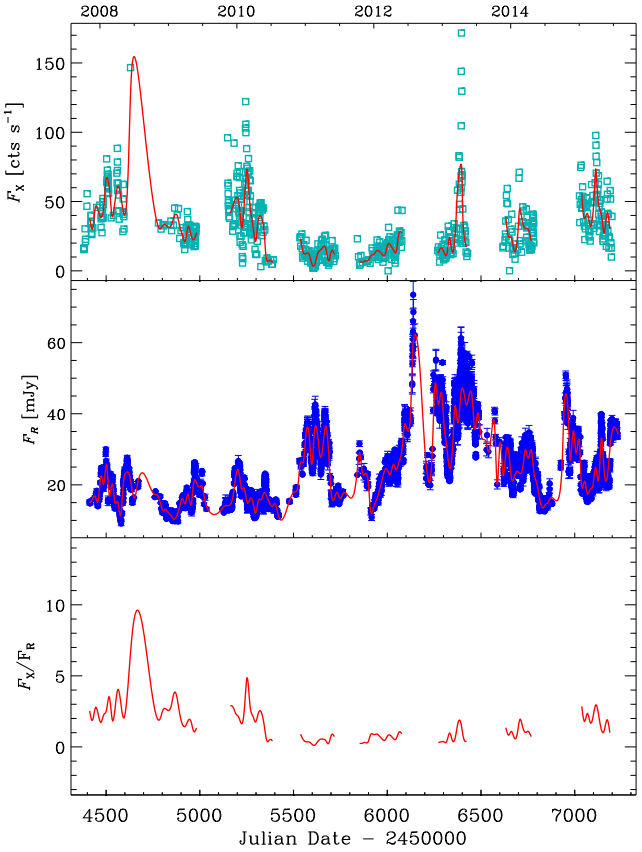

Figure 13. Top panel: the X-ray count rate from *Swift*-XRT. Middle panel: the *R*-band flux densities (mJy). In both panels cubic spline interpolations through the 15-d binned light curves are shown. Bottom panel: the ratio between the X-ray and the optical spline fits.

vector polarization angle (EVPA; e.g. Smith 1996). We analyse the polarimetric behaviour of Mrk 421 by means of 1430 optical data acquired as *R*-band photo-polarimetry by the Lowell (Perkins), Crimean, Calar Alto observatories, and as spectropolarimetry by the Steward Observatory. In the latter case, the values of P and EVPA are derived from the median of the normalized Stokes' parameters $q = Q/I$ and $u = U/I$ in the 5000–7000 Å bandpass, whose effective wavelength is close to the Cousins' R band. A description of the data acquisition and reduction procedures is given in Jorstad et al. (2010), Larionov et al. (2008) and Smith et al. (2003).

The time evolution of the observed P and EVPA is shown in Fig. 14. A cubic spline interpolation through the 15-day binned percentage polarization curve is drawn to highlight the long-term behaviour.

In order to determine the degree of polarization intrinsic to the jet, the unpolarized contribution of the galaxy must be subtracted. The intrinsic polarization is computed using the following expression:

$$P_{\rm jet} = \frac{F_{\rm pol}}{F_{\rm jet}} = \frac{P_{\rm obs} \times F_{\rm obs}}{F_{\rm obs} - F_{\rm gal}}. \quad (1)$$

This is compared to the γ-ray and R-band light curves in Fig. 15.[8] The $\pm 180^\circ n$ (where n is an integer number) ambiguity in EVPA was treated by choosing at each epoch that angle among EVPA,

[8] The number of P data points in Fig. 15 is smaller than in Fig. 14 because to calculate $P_{\rm jet}$ we need $F_{\rm obs}$ (see equation 1), which was not always available.

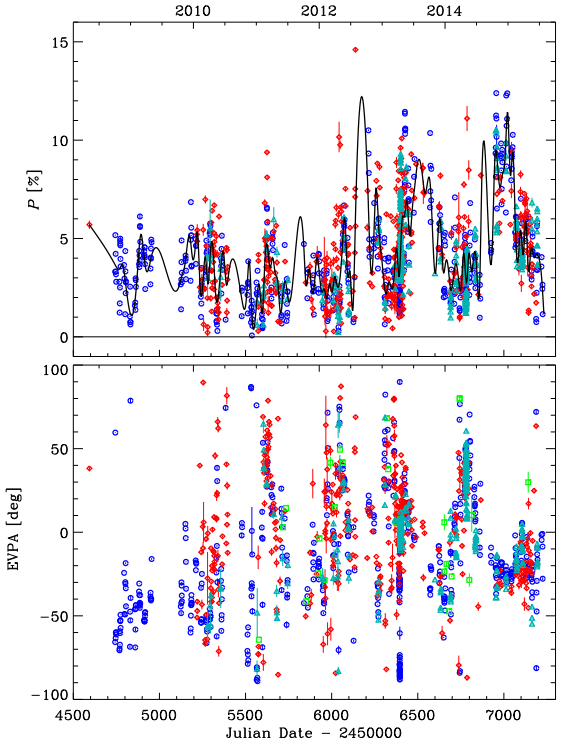

Figure 14. Top panel: the observed degree of polarization as a function of time; the black line represents a cubic spline interpolation through the 15-d binned data. Bottom panel: the observed EVPAs in the -90° and $+90^\circ$ range. Data are from the Calar Alto (green squares), Crimean (red diamonds), Lowell (cyan triangles) and Steward (blue circles) Observatories.

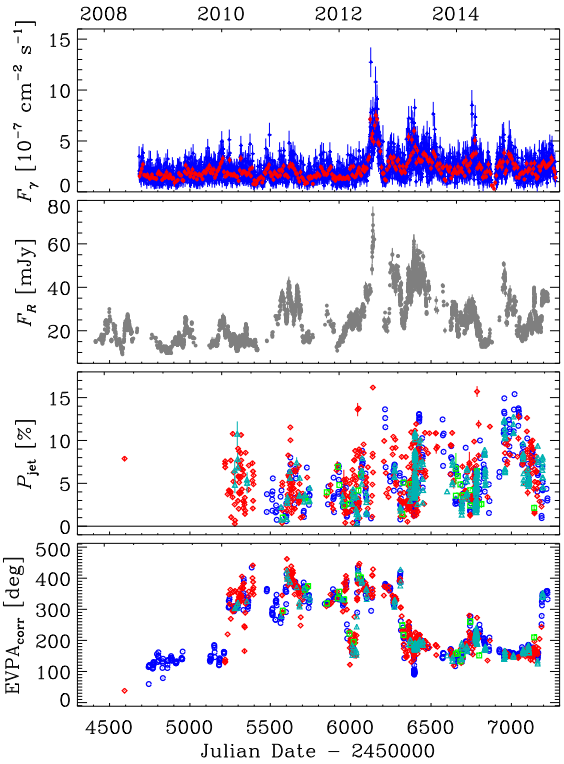

Figure 15. From the top to bottom: the γ-ray fluxes between 100 MeV and 300 GeV; the *R*-band flux densities cleaned from the host-galaxy light contamination; the degree of polarization of the jet emission; the EVPA after fixing the $\pm 180^\circ n$ ambiguity. Symbols and colours as in Fig. 14.

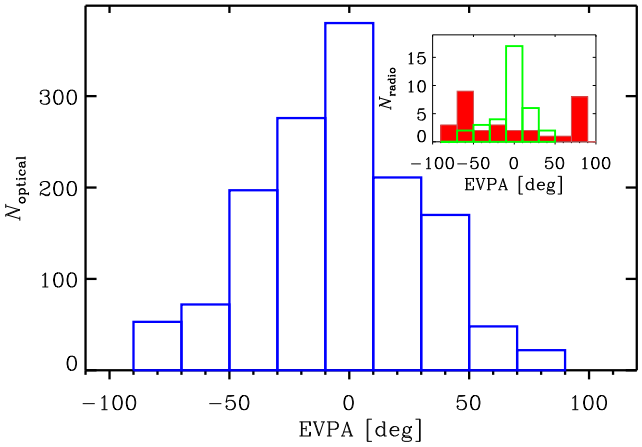

Figure 16. The distribution of the optical EVPAs; the inset displays those of the radio EVPAs at 43 GHz (green line) and at 15 GHz (red histogram).

EVPA+180° and EVPA−180° that leads to a minimum angle difference with respect to the previous epoch. In this choice, we also considered the errors on the EVPAs.

The polarization degree ranges between 0.07 and 14.6 per cent, with a mean value of about 4 per cent. The fractional variability F_{var} (see Section 6.2) for P is ∼0.56, significantly larger than that of both optical and γ-ray fluxes, which is ∼0.40. This suggests that polarization is likely to be dominated by shorter time-scale effects than the optical and γ-ray flux variability. In any case, the figure shows that there are periods where a high flux corresponds to a high polarization degree, but this is not a general rule.

The EVPA values cluster around a mean value of ∼4° (see Fig. 16), but wide rotations appear after arranging the angles to fix the $\pm 180^\circ n$ ambiguity. Fig. 16 also shows the distribution of radio EVPAs at 43 and 15 GHz from the Boston University Blazar Group[9] and MOJAVE Project[10] (Lister et al. 2009), respectively. The number of radio data is small, but they suggest that the direction of the 43 GHz polarization is aligned with the optical one, while the 15 GHz emission, likely coming from an outer jet region, has a transverse polarization angle. A flip by 90° in EVPA usually means that there is a change from optically thin to optically thick properties of the region that most likely has happened between 43 and 15 GHz. In Fig. 17, we plot enlargements of Fig. 15 in different periods to better distinguish the variability properties. We warn that in some cases wide rotations may derive from EVPA shifts performed when the angle difference between subsequent points was around 90°. Though we have considered the angle uncertainties, it is clear that an underestimate of the error in these cases could lead to an apparent wider rotation. This happens in the following dates: JD = 2455234, 2455340 and 2455974. In contrast, there are cases where the rotation appears quite robust. In particular, around JD = 2456040, we observe a counter-clockwise rotation of ∼250° in about 10 d. This happens when P reaches a local maximum of ∼10 per cent and the flux is rising towards the peak of 2012 July and August. Another noticeable episode occurred in the last observing season. The EVPA remained stable for several months, and then rotated by ∼180° in a counter-clockwise direction in about one month around JD = 2457180. We note that P experienced a local minimum at about half-way of the rotation and two symmetric maxima at the beginning and at the end of the rotation. This behaviour has already been observed in 3C 279 and was interpreted by Nalewajko (2010) in terms of an emitting blob encountering a major bending while travelling in the jet. If we apply that model to our case, assuming a Lorentz factor $\Gamma_{jet} = \Gamma_{blob} = 10$, we find a minimum angle between the blob velocity vector and the line of sight of 3.4°, a curvature radius of the trajectory of about 6.6×10^{14} cm, and a distance covered by the blob between the minimum and maximum of P of about 5.3×10^{13} cm. As in the case of 3C 279, the lack of a simultaneous optical flare at the time of the minimum P would mean that the blob gives only a very small contribution to the total observed flux.

In Fig. 18, we show both P_{obs} versus F_{obs} and P_{jet} versus F_{jet}. It can be noticed that in both cases no apparent correlation exists between the two quantities.

Fig. 19 shows the distribution of the Stokes' parameters of Mrk 421 in the u versus q plot, highlighting the EVPA rotation that occurred in 2015 May and June. To this aim, subsequent points have been connected with a cubic spline interpolation. The distance of the spline from the origin, together with the wideness of the spline and the persistence of the direction of rotation, confirms the genuine nature of the rotation.

10 SPECTROPOLARIMETRIC OBSERVATIONS

We analysed 603 spectra from the Steward Observatory data base to investigate the optical spectropolarimetric variability properties of Mrk 421. Fig. 20 shows the source spectra corresponding to the brightest and faintest states. They lack emission lines and point out a bluer-when-brighter behaviour. In the fainter spectrum, we can recognize the Mg I and Na I absorption lines from the host galaxy.

Fig. 21 shows the optical colour of Mrk 421 as a function of the R-band flux density. The colour is determined as the ratio between the median flux in the range 4000–5000 Å ('blue') and that in the 5800–6800 Å range ('red').[11] Here, again we note a bluer-when-brighter trend.

We then investigated the wavelength dependence of the optical polarization. We did not find correlation between the degree of optical linear polarization P and the ratio between the blue and the red fluxes (see Fig. 22).

Fig. 23 shows flux densities and polarization percentages for the two wavelength ranges. The blue side is characterized by higher flux variability and polarization degree than the red one, consistently with the larger contribution of the host galaxy light in the red range.

Fig. 24 shows the flux ratio between the blue and the red bins plotted against the ratio of the observed polarization in the same bins. As the blazar becomes fainter (redder), the polarization in the blue tends to be higher than in the red because of the increasing contribution from the red and unpolarized host galaxy light. However, in the faint states, the low levels of polarization result in relatively large uncertainties in P_{blue}/P_{red}. Fig. 24 also shows the difference between the polarization position angles determined in the two continuum bins. The plot suggests that there is no wavelength dependence in EVPA.

[9] https://www.bu.edu/blazars/research.html
[10] http://www.physics.purdue.edu/MOJAVE/

[11] We could not use the reddest part of the spectra (from 6800 to 7550 Å) because it includes terrestrial oxygen and water absorption features.

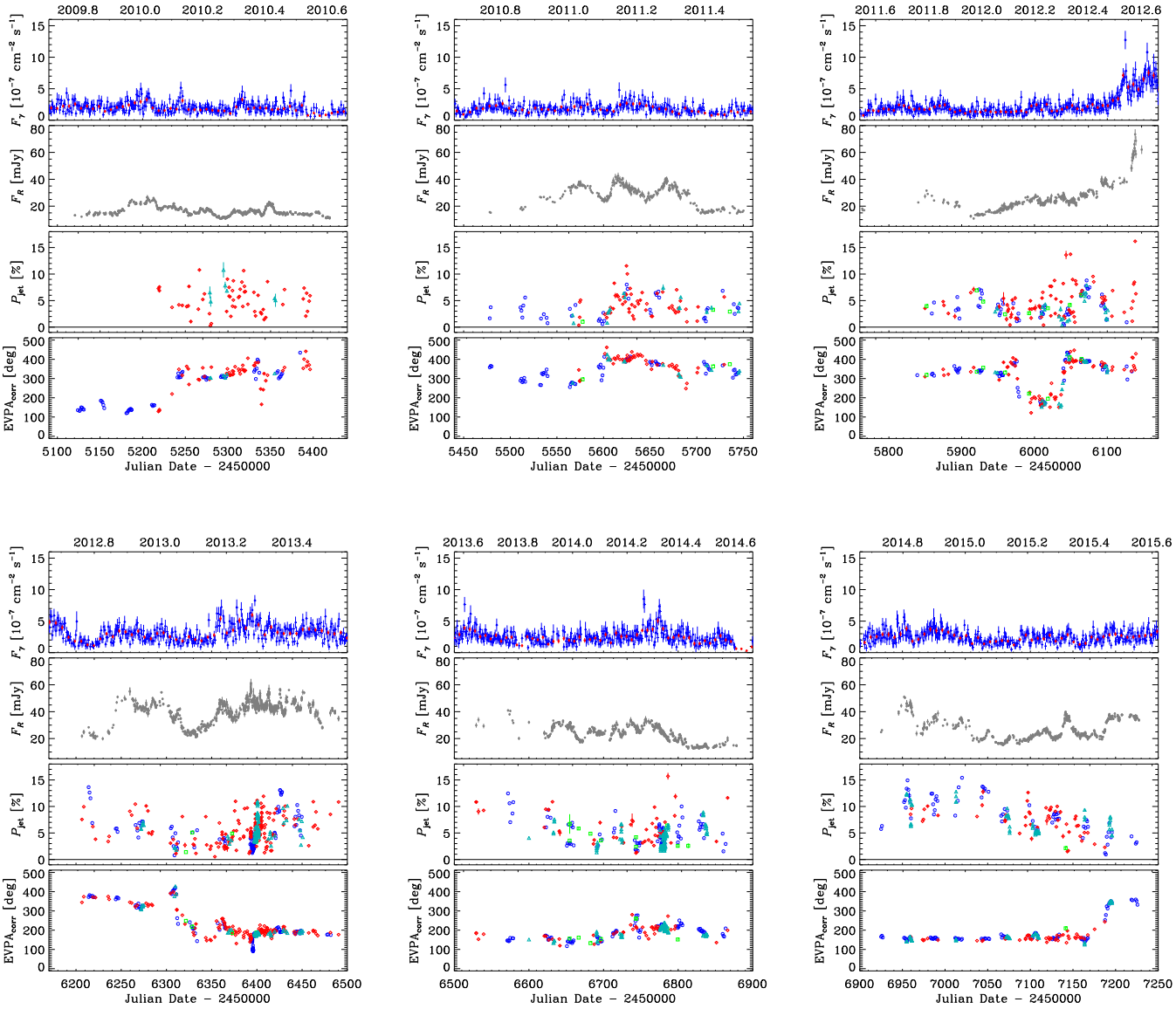

Figure 17. Enlargements of Fig. 15 to appreciate short-term variability.

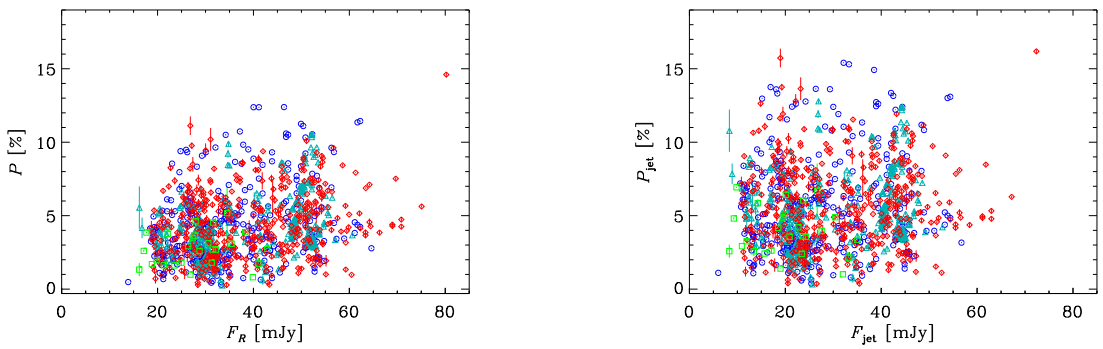

Figure 18. Left-hand panel: The observed degree of polarization as a function of the observed *R*-band flux density. Right-hand panel: The same plot after correcting for the host contribution.

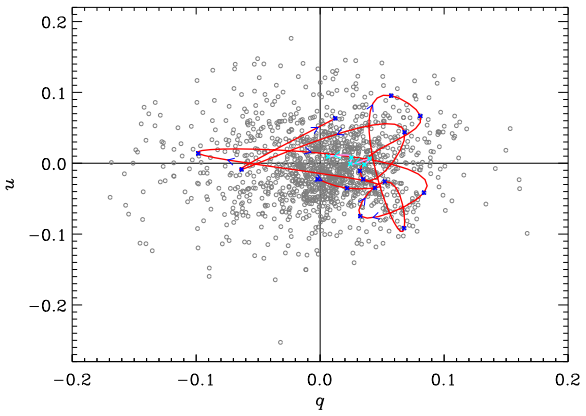

Figure 19. Distribution of the Stokes' parameters in the u versus q plot. The red line highlights the EVPA rotation that occurred in 2015 May and June and was obtained by connecting subsequent points with a cubic spline interpolation. The arrows indicate the time evolution.

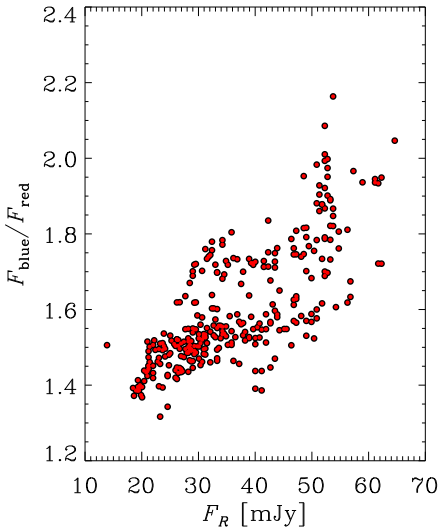

Figure 21. The Mrk 421 optical colour ('blue' to 'red' flux ratio) as a function of the source brightness (observed R-band flux density in mJy).

11 DISCRETE CORRELATION FUNCTION

We apply the discrete correlation function (DCF) analysis to the data shown in Fig. 12 in order to investigate the existence of characteristic time-scales of variability and the correlation between the γ-ray, X-ray and optical fluxes. This method is suitable to treat unevenly sampled data sets (Edelson & Krolik 1988; Hufnagel & Bregman 1992). Correlation/anticorrelation produces a positive/negative peak of the DCF. The correlation is strong if the peak value approaches or even exceeds one.

The DCF between the X-ray and R-band light curves over the whole 2007–2015 period is shown in Fig. 25. The lack of a strong signal suggests that the X-ray and optical variations are, in general, not correlated. The two low peaks at about −130 and −260 d indicate optical events preceding X-ray ones and likely refer to the major flares in 2012–2015.

In the same figure, we show the DCF between the daily binned γ-ray and the X-ray light curves. The central low peak is likely produced by the match of the major X-ray flare of 2013 with a contemporaneous γ-ray flare. Another low peak at a time lag of ∼250 d comes from the correspondence between the major 2012 optical and 2013 X-ray flares. However, the value of the DCF always maintains low, implying that the correlation is weak.

Finally, Fig. 25 displays the DCF between the daily binned γ-ray and the optical fluxes over the whole data trains. The value of the DCF at the central maximum is 0.48 and indicates fair correlation between the flux variations in the γ-ray and optical bands. The central maximum is broad, possibly because of the superposition of different signatures. To check this, we divided the considered period in three subperiods: the time interval before the big 2012 γ-optical outburst (JD < 2456000), the time interval after

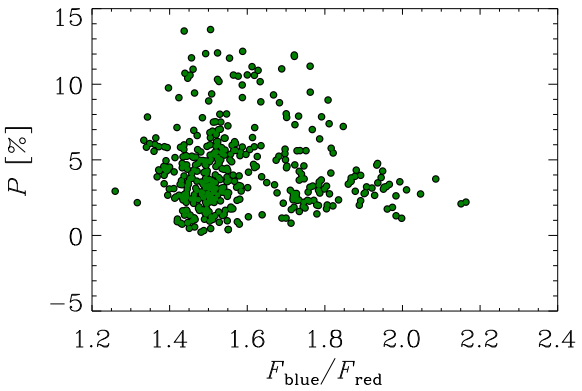

Figure 22. The observed degree of polarization plotted against the optical colour of Mrk 421. The polarization and flux ratio measurements are simultaneous.

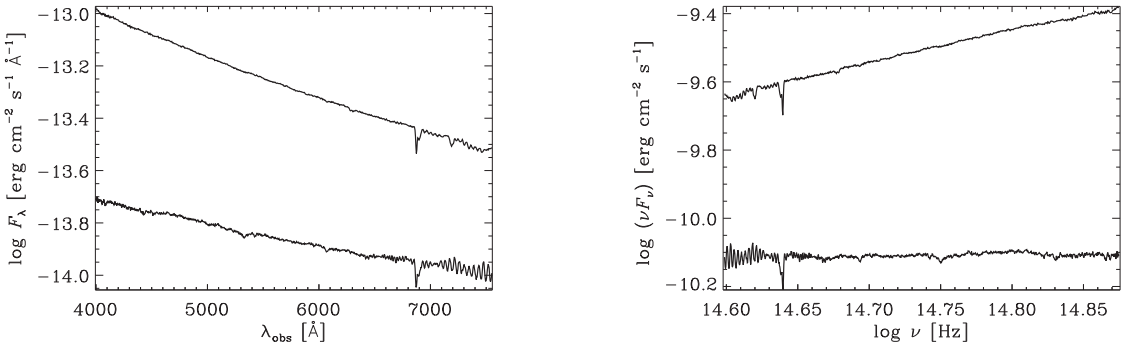

Figure 20. Left-hand panel: the brightest and faintest spectra in the Steward Observatory data base. Their flux density ratio is ∼5. Right-hand panel: the same spectra in the log (νF_ν) versus log ν representation used for the SED.

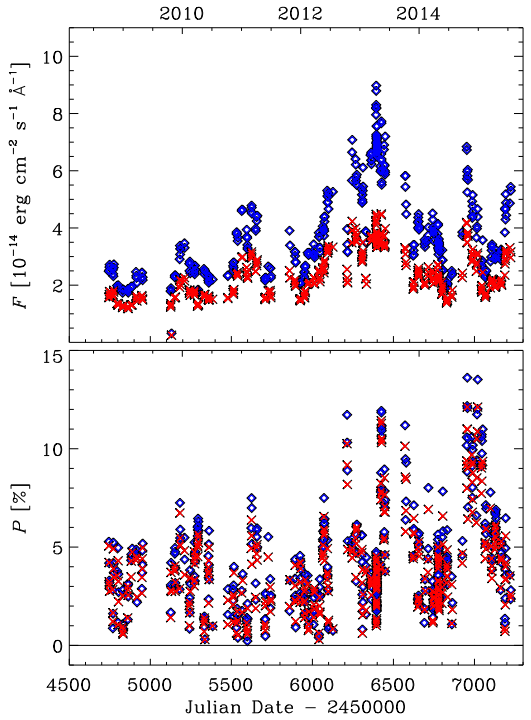

Figure 23. The observed optical flux density (top panel) and polarization percentage (bottom panel) as a function of time in the blue and red bins defined in the text.

the outburst (JD > 2456200) and the time interval including the outburst (2456000 < JD < 2456200). We then calculated the γ-optical cross-correlation for the three periods separately. Before the big outburst, the DCF value is always very low, indicating a poor correlation; after the outburst, the strength of the correlation increases and the central peak (DCF = 0.46) suggests a fair correlation with essentially no time delay. Around the outburst, the correlation is strong, as expected, but the timing is badly defined, with γ variations that can either precede or follow the optical ones. This ambiguity is essentially due to the lack of optical data during the 2012 solar conjunction, when the γ-ray outburst was still at its highest levels.

The optical, X-ray and γ-ray auto correlation functions (ACFs) are plotted in Fig. 26. The peaks are low and their lags reflect the time separation between flares in the corresponding light curves. None of these time-scales can be considered as a periodicity. A recent detailed periodicity analysis on the γ and optical light curves of Mrk 421 by Sandrinelli et al. (2017) found no periodic signals.

12 BROAD-BAND SPECTRAL VARIABILITY

We built IR-to-X-ray SEDs to investigate the spectral variability of Mrk 421 around the synchrotron peak. In order to be able to reliably characterize and model the region of the SED around the synchrotron peak, we considered all the observing epochs where strictly simultaneous data in the *K*, *H*, *J*, *R* bands from the WEBT Collaboration and at UV and X-ray frequencies from the *Swift*

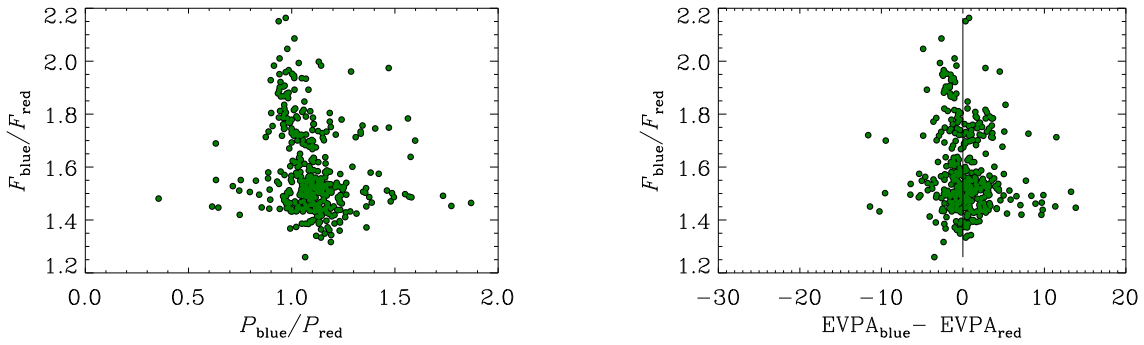

Figure 24. Left-hand panel: the relationship between the ratio of observed polarization in the blue and red bins and the colour defined as in Fig. 21. Right-hand panel: colour versus the difference between the polarization position angles in the blue and red bins.

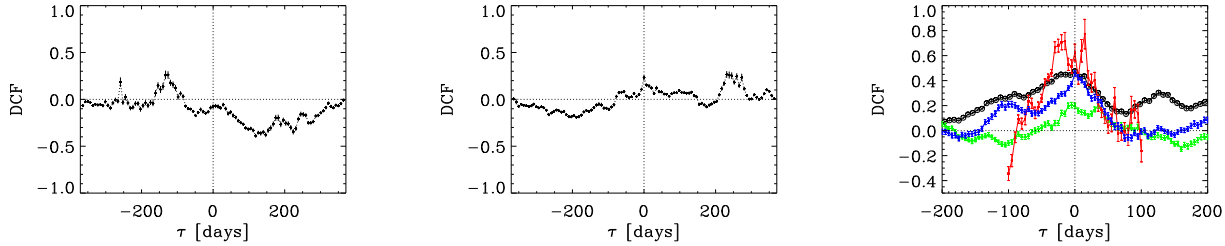

Figure 25. DCF between the X-ray and *R*-band light curves (left-hand panel); the daily binned γ-ray and X-ray light curves (middle panel); the daily binned γ-ray and *R*-band light curves (right-hand panel, empty black circles) over the whole 2007–2015 period. In the last panel, we also show the results of the DCF run on the three subperiods corresponding to the time intervals before the 2012 outburst (green triangles), after the outburst (blue diamonds) and around the outburst (red squares).

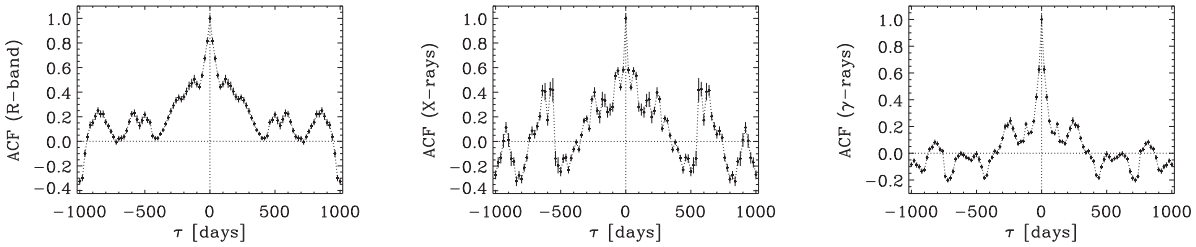

Figure 26. ACF for the galaxy-subtracted optical flux densities (left-hand panel), X-ray count rates (middle panel) and γ-ray fluxes (right-hand panel).

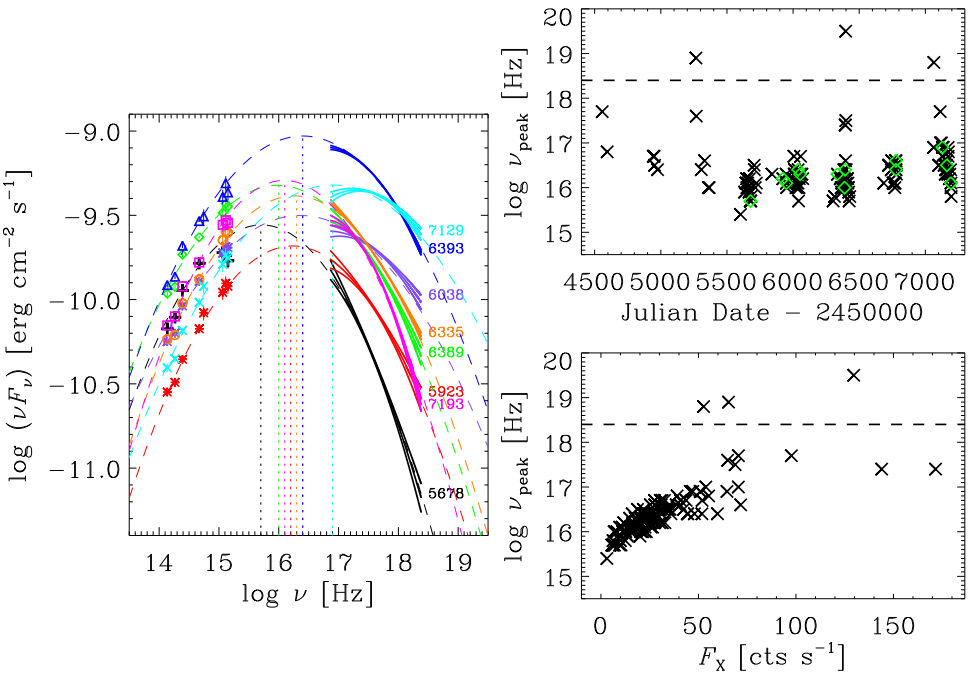

Figure 27. Left-hand panel: broad-band SEDs of Mrk 421 at eight different epochs (identified on the right with their JD − 2450000) where simultaneous near-IR, optical, UV and X-ray data are available. Right-hand panels: The synchrotron peak frequency versus time (top panel) and X-ray flux (bottom panel). The horizontal lines correspond to 10 keV, the upper limit of the energy range covered by XRT. In the top panel, the diamonds represent the cases where also near-IR data were available and included in the SED fit.

satellite were available. Eight of these SEDs[12] are shown in Fig. 27, covering a wide range of brightness states. In three cases, we also found UVOT data in the v band. The errors in the near-IR and optical flux densities are typically around 3 per cent and are included in the symbol size, while we conservatively assumed a 10 per cent error on the UVOT data. The X-ray spectra are the result of a log-parabola model fitting, including the uncertainties on the flux normalization and α and β parameters.

We also show log-parabolic fits to the broad-band SEDs and the position of the synchrotron peak they identify. The X-ray spectral variability is quite strong and suggests that the frequency of the synchrotron peak can shift over a large range, from $\log \nu \sim 15.7$ to 16.9 [Hz]. Taking into account the curvature of the X-ray spectra alone, the range could be even broader, up to $\log \nu \sim 17.4$ of the JD = 2457129 SED, i.e. a factor 50 in frequency. From these few SEDs, the relationship between the brightness state and the synchrotron peak frequency appears confused. In particular, the highest peak frequency (JD = 2457129) does not correspond to the highest X-ray flux (JD = 2456393). To better investigate this point, we built SEDs of all epochs with contemporaneous *Swift* and *R*-band data and fit them with a log-parabolic model. The results are shown in Fig. 27. There is a general indication that the synchrotron peak frequency follows the X-ray activity, shifting towards higher values when the X-ray flux increases. The increase is fast below ∼30 counts s^{-1}, then the curve flattens. Values of $\log \nu_{\rm peak}$ larger than 17 are reached only if the X-ray count rate is greater than 50 counts s^{-1}. Beyond this general behaviour, there are specific cases with peculiar spectral shapes. There are three cases where the X-ray spectrum is hard so that $\nu_{\rm peak}$ falls beyond the 10 keV upper limit of the XRT energy range.

The only steep UV spectrum is shown by the SED on JD = 2455678, corresponding to the faintest and softest X-ray spectrum. We also note that its near-IR and optical part fairly matches that observed at JD = 2457193, but the latter has much brighter UV and X-ray states. If the UV spectrum steepness on JD = 2455678 were real and not due to data uncertainties, its extrapolation to the

[12] The other five SEDs overlap with them and were omitted for sake of clarity.

higher energies would not meet the X-ray spectrum, raising the question whether more than one component is contributing to the source synchrotron flux. The same issue was encountered when comparing the optical and X-ray light curves in Section 8. Similar mismatches in the SED have already been found for this source (Massaro et al. 2004) and were sometimes observed in other HBLs, like PG 1553+113 (Raiteri et al. 2015) and H1722+119 (Ahnen et al. 2016a). In these two cases, they have been interpreted in terms of orientation variations in an inhomogeneous helical jet.

Another pair of SEDs having the same near-IR and optical flux, but a different UV flux and very different X-ray spectra are those on JD = 2456038 and 2456335. Here, a higher UV state corresponds to a softer and less curved X-ray spectrum.

13 SUMMARY AND CONCLUSIONS

In this paper, we have analysed 8 yr of multiwavelength data on the HBL Mrk 421. The GASP-WEBT Collaboration and Steward Observatory provided the near-IR and optical photometric and polarimetric data. Information in the UV and X-ray bands was acquired from the *Swift* satellite and in γ-rays from the LAT instrument onboard *Fermi*. We have also exploited the spectropolarimetric data taken at the Steward Observatory to investigate a possible wavelength dependence of the polarization degree P and angle EVPA. We have calculated the host galaxy contribution to the source photometry in the near-IR, optical and UV bands and subtracted it to analyse the jet emission.

The source showed unceasing activity at all frequencies over all the 2007–2015 period we considered. Variability in the near-IR, UV and γ-ray flux appears well correlated with the optical one, showing prominent flares in 2012–2013. In contrast, the behaviour in X-rays does not follow the same path and X-ray flares occurred in 2008, 2010 and 2013. In γ-rays, the most noticeable event occurred in 2012, while significant flares were also observed in 2013–2014. DCF analysis suggests the lack of a persistent X-ray–optical correlation while indicates a fair correlation between the γ-ray and optical flux changes since 2012.

The spectral variability increases with frequency: Broad-band SEDs show that the near-IR to optical spectral shape is rather stable for different brightness states, while the upturn towards the UV can be more or less pronounced, and this corresponds to a different X-ray spectral form. Indeed, X-ray spectra exhibit a large variety of slopes and curvatures and suggest that the synchrotron peak may cover a large range of frequencies and, in general, shifts towards higher energies when the X-ray flux increases.

The energy output from Mrk 421 has often been interpreted with one-zone SSC models (e.g. Aleksić et al. 2012) or with lepto-hadronic models involving proton synchrotron radiation and/or photopion interactions (e.g. Böttcher et al. 2013). In these models, the variations of the SED shape are obtained by changing the parameters determining the jet physics. In particular, these changes can produce a shift of the synchrotron peak frequency and, in turn, a lack of correlation between the optical and X-ray emission, even if these two emissions are physically connected. Alternatively, we propose the existence of at least two emitting regions in the jet to explain the different behaviour of the optical and X-ray fluxes. These regions are disjointed and experience independent short-term variability. Moreover, their orientation can likely change in time, so that periods of high X-ray activity would be observed when the part of the jet producing this radiation is more closely aligned with the line of sight. Similarly, when the viewing angle of the optical emitting region decreases, the optical flux would be more Doppler enhanced.

We have analysed polarimetric data to look for episodes where the behaviour of P and EVPA can suggest that the source variability is due to geometrical effects, like a curved motion of a blob in a helical jet (Nalewajko 2010). We found a possible candidate in the last part of the campaign, and derived the minimum angle between the blob velocity vector and the line of sight, the curvature radius of the trajectory and the distance covered by the blob during that event. Apart from this case, we have not found any correlation between the source flux, and the P and EVPA changes, which strongly suggests that turbulence may play a major role in determining the source polarimetric properties (Marscher 2014; Blinov et al. 2016; Kiehlmann et al. 2016; Raiteri et al. 2017).

ACKNOWLEDGEMENTS

We are grateful to an anonymous referee for useful comments and suggestions. The data collected by the WEBT collaboration are stored in the WEBT archive at the Osservatorio Astrofisico di Torino – INAF (http://www.oato.inaf.it/blazars/webt/); for questions regarding their availability, contact the WEBT President Massimo Villata (villata@oato.inaf.it). This article is partly based on observations made with the telescopes IAC80 and TCS operated by the Instituto de Astrofísica de Canarias in the Spanish Observatorio del Teide on the island of Tenerife. The IAC team acknowledges the support from the group of support astronomers and telescope operators of the Observatorio del Teide. Based (partly) on data obtained with the STELLA robotic telescopes in Tenerife, an AIP facility jointly operated by AIP and IAC. The Steward Observatory blazar monitoring programme is funded by NASA through Fermi Guest Investigator grants NNX08AW56G, NNX09AU10G, NNX12AO93G and NNX15AU81G. The Abastumani team acknowledges financial support by Shota Rustaveli NSF under contract FR/577/6-320/13. The research at BU was supported in part by US National Science Foundation grant AST-1615796 and NASA Fermi Guest Investigator grant NNX14AQ58G. This study makes use of 43 GHz VLBA data from the VLBA-BU Blazar Monitoring Program (VLBA-BU-BLAZAR; http://www.bu.edu/blazars/VLBAproject.html), funded by NASA through the Fermi Guest Investigator Program. The PRISM camera at the Lowell Observatory was developed by K. Janes et al. at the BU and Lowell Observatory, with funding from the NSF, BU and Lowell Observatory. This research has made use of data from the MOJAVE data base, which is maintained by the MOJAVE team (Lister et al. 2009). The St. Petersburg University team acknowledges support from Russian RFBR grant 15-02-00949 and St. Petersburg University research grant 6.38.335.2015. This paper is partly based on observations carried out at the German-Spanish Calar Alto Observatory, which is jointly operated by the MPIA and the IAA-CSIC. IA research is supported by a Ramón y Cajal grant of the Spanish Ministerio de Economía y Competitividad (MINECO). Acquisition of the MAPCAT data was supported in part by MINECO through grants AYA2010-14844, AYA2013-40825-P and AYA2016-80889-P, and by the Regional Government of Andalucía through grant P09-FQM-4784. This research was partially supported by the Scientific Research Fund of the Bulgarian Ministry of Education and Sciences under grants DO 02-137 (BIn-13/09) and DN 08/1. The Skinakas Observatory is a collaborative project of the University of Crete, the Foundation for Research and Technology – Hellas and the Max-Planck-Institut für Extraterrestrische Physik. GD and OV gratefully acknowledge the observing grant support from the Institute of Astronomy and Rozhen National

Astronomical Observatory, Bulgaria Academy of Sciences, via the bilateral joint research project 'Observations of ICRF radio-sources visible in optical domain' (the head is Dr G. Damljanovic). This work is a part of the Projects No 176011 ('Dynamics and kinematics of celestial bodies and systems'), No 176004 ('Stellar physics') and No 176021 ('Visible and invisible matter in nearby galaxies: theory and observations') supported by the Ministry of Education, Science and Technological Development of the Republic of Serbia. The Serbian station is the Astronomical Station Vidojevica (ASV) with the 60-cm ASV telescope (and from this year, the 1.4-m ASV one). This research was supported partly by funds of the project RD-08-81 of the Shumen University.

REFERENCES

Abdo A. A. et al., 2011, ApJ, 736, 131
Acero F. et al., 2015, ApJS, 218, 23
Aharonian F. et al., 2005, A&A, 437, 95
Ahnen M. L. et al., 2016, MNRAS, 459, 3271
Ahnen M. L. et al., 2016, A&A, 593, A91
Albert J. et al., 2007, ApJ, 663, 125
Aleksić J. et al., 2012, A&A, 542, A100
Aleksić J. et al., 2015, A&A, 576, A126
Aleksić J. et al., 2015, A&A, 578, A22
Atwood W. B. et al., 2009, ApJ, 697, 1071
Atwood W. et al., 2013, in Brandt T. J., Omodei N., Wilson-Hodge C., eds., Proc. of the 4th Fermi Symposium, Monterey, California
Baloković M. et al., 2016, ApJ, 819, 156
Bessell M. S., Castelli F., Plez B., 1998, A&A, 333, 231
Blasi M. G. et al., 2013, A&A, 559, A75
Blinov D. et al., 2016, MNRAS, 462, 1775
Böttcher M., Reimer A., Sweeney K., Prakash A., 2013, ApJ, 768, 54
Burrows D. N. et al., 2005, Space Sci. Rev., 120, 165
Cardelli J. A., Clayton G. C., Mathis J. S., 1989, ApJ, 345, 245
Carnerero M. I. et al., 2015, MNRAS, 450, 2677
Carnerero M., Raiteri C., Villata M., Acosta Pulido J., Smith P., Larionov V., 2016, Galaxies, 4, 61
Donnarumma I. et al., 2009, ApJ, 691, L13
Edelson R. A., Krolik J. H., 1988, ApJ, 333, 646
Hartman R. C. et al., 1999, ApJS, 123, 79
Hovatta T. et al., 2015, MNRAS, 448, 3121
Hufnagel B. R., Bregman J. N., 1992, ApJ, 386, 473
Ikejiri Y. et al., 2011, PASJ, 63, 639
Jorstad S. G. et al., 2010, ApJ, 715, 362
Kapanadze B. et al., 2016, ApJ, 831, 102
Kiehlmann S. et al., 2016, A&A, 590, A10
Larionov V. M. et al., 2008, A&A, 492, 389
Lico R. et al., 2014, A&A, 571, A54
Lister M. L. et al., 2009, AJ, 137, 3718-3729
Lockman F. J., Savage B. D., 1995, ApJS, 97, 1
Mannucci F., Basile F., Poggianti B. M., Cimatti A., Daddi E., Pozzetti L., Vanzi L., 2001, MNRAS, 326, 745
Marscher A. P., 2014, ApJ, 780, 87
Massaro E., Perri M., Giommi P., Nesci R., 2004, A&A, 413, 489
Mattox J. R. et al., 1996, ApJ, 461, 396
Miller H. R., 1975, ApJ, 201, L109
Nalewajko K., 2010, Int. J. Mod. Phys. D, 19, 701
Nilsson K., Pasanen M., Takalo L. O., Lindfors E., Berdyugin A., Ciprini S., Pforr J., 2007, A&A, 475, 199
Paliya V. S., Böttcher M., Diltz C., Stalin C. S., Sahayanathan S., Ravikumar C. D., 2015, ApJ, 811, 143
Peterson B. M., 2001, in Aretxaga I., Kunth D., Mújica R., eds., Advanced Lectures on the Starburst-AGN Connection. World Scientific, Singapore, p. 3
Pian E. et al., 2014, A&A, 570, A77
Piner B. G., Pant N., Edwards P. G., 2010, ApJ, 723, 1150
Polletta M. et al., 2007, ApJ, 663, 81
Punch M. et al., 1992, Nature, 358, 477
Raiteri C. M. et al., 2010, A&A, 524, A43
Raiteri C. M. et al., 2015, MNRAS, 454, 353
Raiteri C. M. et al., 2017, MNRAS, 466, 3762
Roming P. W. A. et al., 2005, Space Sci. Rev., 120, 95
Sandrinelli A. et al., 2017, A&A, 600, A132
Schlegel D. J., Finkbeiner D. P., Davis M., 1998, ApJ, 500, 525
Sinha A., Shukla A., Misra R., Chitnis V. R., Rao A. R., Acharya B. S., 2015, A&A, 580, A100
Skrutskie M. F. et al., 2006, AJ, 131, 1163
Smith A. G., 1996, in Miller H. R., Webb J. R., Noble J. C., eds., ASP Conf. Ser., Vol. 110, Blazar Continuum Variability. Astron. Soc. Pac., San Francisco, p. 3
Smith P. S., Schmidt G. D., Hines D. C., Foltz C. B., 2003, ApJ, 593, 676
Ulrich M.-H., Kinman T. D., Lynds C. R., Rieke G. H., Ekers R. D., 1975, ApJ, 198, 261
Villata M., Raiteri C. M., Lanteri L., Sobrito G., Cavallone M., 1998, A&AS, 130, 305
Villata M. et al., 2009, A&A, 504, L9
Villata M. et al., 2009, A&A, 501, 455
Visvanathan N., Wills B. J., 1998, AJ, 116, 2119
Wilms J., Allen A., McCray R., 2000, ApJ, 542, 914

[1]*INAF, Osservatorio Astrofisico di Torino, via Osservatorio 20, I-10025 Pino Torinese, Italy*
[2]*Instituto de Astrofisica de Canarias (IAC), La Laguna, E-38200 Tenerife, Spain*
[3]*Departamento de Astrofisica, Universidad de La Laguna, La Laguna, E-38205 Tenerife, Spain*
[4]*Astronomical Institute, St. Petersburg State University, Universitetsky pr. 28, Petrodvoretz, 198504 St. Petersburg, Russia*
[5]*Pulkovo Observatory, 196140 St. Petersburg, Russia*
[6]*Steward Observatory, University of Arizona, Tucson, AZ 85721, USA*
[7]*INAF, Istituto di Radioastronomia, via Gobetti 101, I-40129 Bologna, Italy*
[8]*DIFA, Universitá di Bologna, Viale B. Pichat 6/2, I-40127 Bologna, Italy*
[9]*Instituto de Astrofísica de Andalucía, CSIC, Apartado 3004, E-18080 Granada, Spain*
[10]*Institute of Astronomy and NAO, Bulgarian Academy of Sciences, 72 Tsarigradsko shosse Blvd., 1784 Sofia, Bulgaria*
[11]*Department of Physics, Salt Lake Community College, Salt Lake City, UT 84070, USA*
[12]*Department of Astronomy, Faculty of Physics, Sofia University, BG-1164 Sofia, Bulgaria*
[13]*EPT Observatories, Tijarafe, E-38780 La Palma, Spain*
[14]*INAF, TNG Fundación Galileo Galilei, E-38712 La Palma, Spain*
[15]*Max-Planck-Institut für Radioastronomie, Auf dem Hügel, 69, D-53121, Bonn, Germany*
[16]*Graduate Institute of Astronomy, National Central University, 300 Jhongda Road, Jhongli City, Taoyuan County 32001, Taiwan, Republic of China*
[17]*Astronomical Observatory, Volgina 7, 11060 Belgrade, Serbia*
[18]*Agrupació Astronòmica de Sabadell, E-08200 Sabadell, Spain*
[19]*Department of Physics and Astronomy, Brigham Young University, Provo, UT 84602, USA*
[20]*Department of Theoretical and Applied Physics, University of Shumen, 9712 Shumen, Bulgaria*
[21]*School of Cosmic Physics, Dublin Institute For Advanced Studies, D02 XF86, Dublin 2, Ireland*
[22]*Institute for Astrophysical Research, Boston University, 725 Commonwealth Avenue, Boston, MA 02215, USA*
[23]*Abastumani Observatory, Mt. Kanobili, 0301 Abastumani, Georgia*
[24]*Engelhardt Astronomical Observatory, Kazan Federal University, 422526 Zelenodolsky region, Tatarstan, Russia*

[25]*Center for Astrophysics, Guangzhou University, Guangzhou 510006, China*
[26]*Circolo Astrofili Talmassons, I-33030 Talmassons, Italy*
[27]*UCD School of Physics, University College Dublin, Dublin 4, Ireland*
[28]*Finnish Centre for Astronomy with ESO (FINCA), University of Turku, FI-21500 Piikkiö, Finland*
[29]*Department of Physical Science, Southern Utah University, Cedar City, UT 84721, USA*
[30]*Osservatorio Astronomico Sirio, Piazzale Anelli, I-70013 Castellana Grotte, Italy*
[31]*Department of Physics, University of Colorado Denver, CO 80217-3364 USA*
[32]*Cork Institute of Technology, Bishopstown, T12 P928 Cork, Ireland*

This paper has been typeset from a TEX/LATEX file prepared by the author.